

Triggered star formation in bright-rimmed clouds: the Eagle nebula revisited

J. Miao,^{1*} Glenn J. White,¹ R. Nelson,² M. Thompson³ and L. Morgan¹

¹Centre for Astrophysics & Planetary Science, School of Physical Science, University of Kent, Canterbury, Kent CT2 7NR

²School of Mathematical Sciences, Queen Mary, University of London, Mile End Road, London E1 4NS

³School of Physics, Astronomy and Mathematics, University of Hertfordshire, College Lane, Hatfield, Herts AL10 9AB

Accepted 2006 March 1. Received 2006 January 5; in original form 2005 June 9

ABSTRACT

A three-dimensional smoothed particle hydrodynamics model has been extended to study the radiation-driven implosion effect of massive stars on the dynamical evolution of surrounding molecular clouds. The new elements in the upgraded code are the inclusion of Lyman continuum in the incident radiation flux and the treatment of hydrogen ionization process; the introduction of ionization heating and recombination cooling effects; and the addition of a proper description of the magnetic and turbulent pressures to the internal pressure of the molecular cloud. This extended code not only provides a realistic model to trace the dynamical evolution of a molecular cloud, but also can be used to model the kinematics of the ionization and shock fronts and the photoevaporating gas surrounding the molecular cloud, which the previous code is unable to handle.

The application of this newly developed model to the structure of the middle Eagle nebula finger suggests that the shock induced by the ionizing radiation at the front side of the head precedes an ionization front moving towards the centre of the core, and that the core at the fingertip is at a transition stage evolving toward a state of induced star formation. The dynamical evolution of the velocity field of the simulated cloud structure is discussed to illustrate the role of the self-gravity and the different cloud morphologies which appear at different stages in the evolutionary process of the cloud. The motion of the ionization front and the evaporating gas are also investigated. The modelled gas evaporation rate is consistent with that of other current models and the density, temperature and chemical profiles are in agreement with the observed values.

The relative lifetimes of different simulated cloud morphologies suggest a possible answer to the question of why more bright-rimmed clouds are observed to possess a flat-core than an elongated-core morphology.

Key words: radiative transfer – stars: formation – ISM: evolution – H II regions – ISM: kinematics and dynamics.

1 INTRODUCTION

The Eagle nebula (M16) presents an excellent laboratory in which to study the influence on star formation due to the presence of nearby massive stars, which can lead to radiative implosion of surrounding molecular cores and the initiation of secondary star formation (Bertoldi 1989; Lefloch & Lazareff 1994). The intriguing structures in the heads of the Elephant Trunks in the Eagle nebula have inspired many studies. A comprehensive survey conducted by Hester et al. (1996) using the *Hubble Space Telescope* (*HST*) Wide Field

and Planetary Camera (WFPC2) resolved a number of evaporating gaseous globules (EGGs) at the tips of finger-like features protruding from columns of cold gas and dust in the Eagle nebula (Hester et al. 1996). More investigations on the physical characteristics and the future evolution of the head structures have also been carried out since then (White et al. 1999; Williams, Ward-Thompson & Whitworth 2001; Fukuda, Hanawa & Sugitani 2002; Sugitani, Tamura & Nakajima 2002; Thompson, Smith & Hester 2002; Urquhart et al. 2003).

In one of our early papers (White et al. 1999), we reported molecular line, millimetre/submillimetre continuum and mid-infrared observations of this region. The steady state of the head structure of the middle finger of the Eagle nebula was estimated using a

*E-mail: j.miao@kent.ac.uk

smoothed particle hydrodynamics (SPH) model which included a simple treatment of an isotropic far-ultraviolet (FUV) radiation field ($6.5 < h\nu < 13.6$ eV). The comparison of the estimated steady state of the head structure of the middle finger with the observed data suggested that the FUV ionization-induced shock might have not passed the core at the middle fingertip, so that the head structure of the fingertip could not be taken as the remains of radiation-driven implosion. The observations revealed that the core structure shows characteristics similar to those expected in the earliest stages of protostellar formation, and therefore it was suspected that the head structure of the middle finger in the Eagle nebula might have evolved from a large and dense structure which existed prior to the expansion of the H II region.

Recently there have been other observations that have supported the idea of triggered protostellar formation at the tip of the middle finger, following the interaction of the natal molecular cloud with the ionizing radiation from the nearby OB stars (Fukuda et al. 2002; McCaughrean & Andersen 2002; Sugitani et al. 2002; Thompson et al. 2002). The question is whether or not ultraviolet radiation from the nearby massive stars could trigger the collapse of the head structures in the Eagle nebula and lead to the next generation of star formation. The challenge is to develop theoretical models that provide a reliable description of the dynamical evolution of these clumpy structures, and which can trace back the history of the clumps, accommodate the current observations, and predict the future evolution of these fingertip structures.

A precise description of the genesis and the future evolution of head structures such as those of the Eagle nebula fingers requires a more rigorous dynamical modelling which should include Lyman continuum in the external radiation field, since hydrogen ionization ought to play a dominant role in the dynamical evolution of molecular cloud structures like those in the Eagle nebula.

A substantial amount of theoretical work has already been carried out to investigate the evolution of dense, gaseous clumps that are in the vicinity of massive OB stars. These include the radiation-driven implosion (RDI) mechanism (Bertoldi 1989), which was developed using an approximate analytical solution for the evolution of a spherically symmetric neutral cloud subject to the radiation of a newly formed nearby star; and the cometary globule model (Lefloch & Lazareff 1994, 1995), which describes the dynamical evolution of a neutral globule illuminated by the ionizing radiation of OB stars based on two-dimensional hydrodynamical simulations. Although these two-dimensional models successfully reproduced some of the observed characteristics of objects influenced by nearby massive stars, they did not adequately include self-gravity (Bertoldi 1989), or self-consistently treat the chemistry and thermal evolution (Lefloch & Lazareff 1994, 1995). Consequently they are unable to deal with the details of triggered star formation by ultraviolet radiation.

Williams et al. (2001) presented a two-dimensional (i.e. cylindrical symmetry of the cloud structure is used) hydrodynamical simulation of the evolution of photoionized clumps with similar characteristics to those found in the Eagle nebula. The simulated results over a variety of initial conditions proposed a different evolutionary scenario from that of White et al. (1999) for the head structures, suggesting that the head structures at the tips of the Eagle nebula trunks may have already survived the propagating shock induced by the external ultraviolet radiation field and are in a near-equilibrium state about 10^5 yr later. In this modelling, self-gravity of the molecular gas was also not included.

The existing discrepancy in the descriptions of the structure of the heads at the fingertips and the recently reported new observations

on the structure of the fingertips suggests the necessity of revisiting the issue of ultraviolet radiation triggered star formation at these fingertips. In order to do this, a self-consistent and comprehensive three-dimensional bright-rimmed cloud (BRC) model is required which can be used to study the ultraviolet radiation triggered star formation in BRCs, and which more generally can be used to describe observations in all BRCs, proplyds and H II regions, to meet the ever-increasing interest in the investigation of the nature of BRCs and proplyds in H II regions. It is obvious from the above that this fully three-dimensional BRC model should be able self-consistently and simultaneously to treat the self-gravity, thermal evolution, radiative transfer and chemistry. Therefore it is our intention to develop the first self-consistent and comprehensive three-dimensional BRC model based on a previous three-dimensional SPH code, which was originally developed to investigate the evolution of isolated molecular clouds under the effect of the interstellar medium radiation (Nelson & Langer 1997).

In the following sections in the present paper we first present an outline for the previous three-dimensional SPH model and then introduce new elements necessary for simulating the evolution of BRCs. The simulation results are discussed and compared with observations, and the evolution of the simulated cloud structure is investigated. A comparison of the results with those based on the previous code is made and then we infer the future evolution of the Eagle nebula finger from its current state. Based on the good agreement between simulations and observations, a reasonable explanation for the observed outnumbered flat-core BRCs is proposed.

2 THE THREE-DIMENSIONAL SPH MODELLING

The physical properties of the head structure of the Eagle nebula presented in our previous paper (White et al. 1999) were based on the SPH code developed by Nelson & Langer (1997), which self-consistently treats the self-gravitational, chemical and thermal evolution in the molecular cloud. We started with a cylindrical finger of radius 0.1 pc with a spherical molecular cloud of $31 M_{\odot}$ at its head, which is under the effect of a FUV radiation field (with photon energy lower than 13.6 eV and enhanced from the $+z$ -direction). Based on an assumed static density distribution (i.e. under the assumption of equilibrium), the temperature and chemical distributions, after the FUV radiation is switched on for 10^5 yr, showed similar characteristics to observations of the middle finger. However, the detailed and accurate description of the whole dynamical evolution, especially of the genesis and future evolution of the observed structures, was not discussed at that time, since the original SPH code did not include the hydrogen ionizing influence of the Lyman continuum radiation ($h\nu \geq 13.6$ eV), the ionization heating, the recombination cooling or the relevant radiative transfer process. These are clearly important, since the effect of the ultraviolet radiation of nearby massive stars on their surrounding molecular clouds tells us that hydrogen ionization is one of the most important physical processes in RDI models (Bertoldi 1989; Lefloch & Lazareff 1994; Williams et al. 2001).

Recently, Kessel-Deynet & Burkert (2000, 2003) have developed a three-dimensional SPH model of the RDI of molecular clouds which includes both self-gravity and hydrogen ionization from nearby stars. Their model has provided the first 3D SPH code to treat ionizing radiation in turbulent astrophysical fluid flows, opening up a wide field of applications involving feedback processes of young massive stars on their parental clouds. However, a self-consistent treatment for the thermal evolution was not included in

this model, and the energy evolution was approximated by a simple linear function of the ionization ratio x , i.e. $E = xE_{10000} + (1 - x)E_{\text{cloud}}$, where E is the internal energy of a representative particle with ionization ratio x (E_{10000} being the internal energy of a fully ionized particle at a temperature of 10 000 K and E_{cloud} being the internal energy of a neutral particle at a temperature of 10 K). The absence of a self-consistent treatment of the ionization heating and recombination cooling processes in their model prevents a rigorous calculation of the physical properties of the cloud, such as gas temperature, density, sound velocity and pressure (Kessel-Deynet & Burkert 2000, 2003), which in fact can adequately be validated through observational data.

We therefore extend our previous code to include a wider range of ultraviolet radiation energy distributions, hydrogen ionization, radiative transfer, ionization heating and recombination cooling, to provide a more comprehensive and self-consistent investigation of the effect of radiation of massive stars on their parental molecular clouds.

2.1 The main components in the previous SPH code

A detailed description of the previous SPH code can be found in Nelson & Langer (1997) and White et al. (1999). Here we present a brief introduction of its main features for completeness. In the previous version of the code, the SPH numerical technique was employed to solve the following continuity, momentum and energy equations for a compressible fluid:

$$\frac{d\rho}{dt} + \rho \nabla \cdot \mathbf{v} = 0, \quad (1)$$

$$\frac{d\mathbf{v}}{dt} = -\frac{1}{\rho} \nabla P - \nabla \Phi + \mathbf{S}_{\text{visc}}, \quad (2)$$

$$\frac{d\mathcal{U}}{dt} + \frac{P}{\rho} \nabla \cdot \mathbf{v} = \frac{\Gamma - \Lambda}{\rho}, \quad (3)$$

and the chemical rate equations take the general form

$$\frac{dX_i}{dt} = nK_i, \quad (4)$$

where $d/dt = \partial/\partial t + \mathbf{v} \cdot \nabla$ denotes the convective derivative, ρ is the density, \mathbf{v} is the velocity, P is the pressure, \mathbf{S}_{visc} represents the viscous forces, \mathcal{U} is the internal energy per unit mass, and Φ is the gravitational potential. Γ and Λ represent non-adiabatic heating and cooling functions respectively.

The heating function Γ in thermal modelling is mainly provided by the photoelectric emission of electrons from grains illuminated by the incident FUV ($6.5 < h\nu < 13.6$ eV) component at the surface of the cloud. This is stronger on the surface facing toward the source star, and weaker on the shielded cloud surface since the latter is mainly from backscattered light from the surrounding interstellar medium and is ~ 0.1 – 0.2 times that on the directly illuminated surface (Désert, Boulanger & Puget 1990; Hurwitz, Bowyer & Martin 1991), i.e. the FUV radiation flux incident on the boundary of the cloud can be written as

$$J_{\text{FUV}}(r = R, \theta) = \begin{cases} 2000G_0, & 0^\circ \leq \theta \leq 90^\circ, \\ 0.2 \times 2000G_0, & 90^\circ \leq \theta \leq 180^\circ, \end{cases}$$

where G_0 is the standard interstellar ultraviolet field (Habing 1968) and θ is the azimuthal angle in spherical coordinates. Heating of the gas is also affected by cosmic ray heating, H_2 formation heating and gas–dust thermal exchange.

The cooling function Λ is affected by CO, C I, C II and O I line emission. The fractional abundances of the main chemical species X_i in equation (4) are for CO, C I, C II, HCO^+ , O I, H^+ , H_3^+ , $\text{OH}_{1,2}$, $\text{CH}_{1,2}$, M^+ and electrons; K_i is the associated chemical reaction rate and n is the total number density. Detailed formulae for these physical and chemical processes can be found in the papers of Nelson & Langer (1997) and White et al. (1999).

The dominant heating process included in the above is the photoelectric emission of electrons from dust grains by the incident FUV (1 – 13.6 eV), as the code was originally developed to observe the influence of the interstellar radiation on the chemical and thermal evolution of isolated molecular clouds, such as Bok globules. For the investigation of the influence of more intensive ultraviolet radiation from massive stars on the evolution of its surrounding objects, hydrogen ionization heating will play a dominant role because of the intensive Lyman continuum photons available in the radiative flux, and the much higher abundance of hydrogen atoms than of grain particles. Therefore it is necessary to include the hydrogen ionization process and the relevant heating and cooling process in order to meet our goal.

2.2 New elements

The new elements added into the above original code solve for the ionizing radiation transfer equation, hydrogen ionization heating and electron recombination cooling. We also introduce a realistic description of the pressure of the molecular cloud by including the turbulent and magnetic pressures. More detailed descriptions are contained in the following subsections.

2.2.1 Ionizing radiation transfer

Although helium ionization has been included in the above chemical network, we could safely neglect it when dealing with the ionization radiation transfer, ionization heating and cooling for simplicity, because of the much lower abundance of helium compared with hydrogen atoms (Dyson & Williams 1997). The treatment of ionizing radiation from nearby stars in the above SPH code is based on solving the following ionization rate and radiative transfer equations:

$$\begin{aligned} \frac{dn_e}{dt} &= \mathcal{I} - \mathcal{R}, \\ \frac{dJ}{dz} &= -\sigma n(1-x)J, \end{aligned} \quad (5)$$

where $n_e = xn$ is the electron density and x is the ionization fraction; $\mathcal{I} = \sigma n(1-x)J$ is the ionization rate, J is the flux of Lyman continuum photons at the site and σ is the ionization cross-section of hydrogen in the ground state. $\mathcal{R} = n_e^2 \alpha_B = x^2 n^2 \alpha_B$ is the recombination rate, where α_B is the effective recombination coefficient under the assumption of the ‘on the spot’ approximation (Dyson & Williams 1997). In its original definition, the recombination coefficient

$$\alpha = \sum_i \alpha_i$$

includes all of the individual recombination coefficients α_i into the hydrogen atomic energy level i . In the ‘on the spot’ assumption, recombinations into the ground level ($i = 1$) do not lead to any net effect on the change in ionization rate, since the photons released from this recombination process are able to reionize other hydrogen atoms on the spot. Therefore α_1 can be neglected and the resulting

net recombination coefficient can be written as

$$\alpha_B = \sum_{i=2}^{\infty} \alpha_i.$$

The dependence of the recombination coefficient α_B on the temperature can be expressed by (Hummer & Seaton 1963)

$$\alpha_B = 1.627 \times 10^{-13} t_e^{-1/2} (1 - 1.657 \log_{10} t_e + 0.584 t_e^{1/3}), \quad (6)$$

where $t_e = 10^{-4} T$ (T in K).

The equations (6) are numerically integrated at each time-step and with the density distribution $n_H(x, y, z)$ which results from the dynamical evolution. The flux of Lyman continuum photons at the surface of the molecular cloud is taken as $J_0 = 1.5 \times 10^{11} \text{ cm}^{-2} \text{ s}^{-1}$, which is the same as that used by Williams et al. (2001).

2.2.2 Ionization heating and recombination cooling

The implementation of the thermal model for the ionization process includes the energy input by photoionization and energy loss by recombination. When an atom with ionization energy E_1 is ionized following the absorption of one photon of frequency ν and energy $E = h\nu$, it releases one electron which carries the excess kinetic energy $E_\nu - E_1$ which will be transferred to the gas through collisions with other gas particles. The resulting heating rate is described by the following equation:

$$\Gamma_{\text{ionizing}} = n(1-x)\sigma J k T_*, \quad (7)$$

where k is the Boltzmann constant and T_* is expressed as (Cantó et al. 1998)

$$T_* = T_{\text{eff}} \frac{x_0^2 + 4x_0 + 6}{x_0^2 + 2x_0 + 2}, \quad (8)$$

where T_{eff} is the stellar temperature, and $x_0 = h\nu_0/kT_{\text{eff}}$ with ν_0 being the frequency of the Lyman limit.

When a free electron in the plasma is captured by a proton, a photon is emitted and an amount of energy $E_1 + m_e v_c^2/2$ is removed from the internal energy of the gas. The cooling rate due to this process is (Hummer & Seaton 1963)

$$\Lambda_{\text{rec}} = \beta_B n^2 x^2 k T, \quad (9)$$

where $\beta_B = \alpha_B(1 + 0.158 t_e)$.

2.2.3 Cooling by collisionally excited line radiation

Accompanying the ionization of hydrogen atoms, oxygen is ionized to O^+ (O II) as well. Consequently, the collisional excitation of low-lying energy levels of O II has a significant cooling effect in spite of the low abundance of O II , since O II has energy levels with excitation potentials of the order of kT . We use the following simplified formula derived by Raga et al. (2002) to calculate the cooling rate due to the collisional excitation of O II :

$$\Lambda_{\text{colli}} = \Lambda_{\text{colli}(1)} + \Lambda_{\text{colli}(2)}, \quad (10)$$

with

$$\log_{10} \left[\frac{\Lambda_{\text{colli}(1)}}{n_e n_{\text{O II}}} \right] = 7.9 t_1 - 26.8, \quad (11)$$

$$\log_{10} \left[\frac{\Lambda_{\text{colli}(2)}}{n_e n_{\text{O II}}} \right] = 1.9 \frac{t_2}{|t_2|^{0.5}} - 20.5, \quad (12)$$

with $t_1 = 1-2000 \text{ K}/T$, $t_2 = 1-5 \times 10^4 \text{ K}/T$ and $n_{\text{O II}} = x n_{\text{O}}$. The above formula is valid in the limit of low electron density $n_e < 10^4 \text{ cm}^{-3}$, which is true for the BRC systems.

2.2.4 The pressure of the cloud and the boundary conditions

At the start of a simulation, the molecular cloud is assumed to have a spherical symmetry which is the general assumption adopted by most existing theoretical models as the initial morphology of the molecular cloud. The geometrical evolution of an initially spherical molecular cloud under the effect of external environments may provide a platform for us to investigate the influence of the external radiation field on the morphology of the cloud. For investigation of the star formation at the tips of the Eagle nebula fingers, it is the dynamical evolution of the head structure which interests us, therefore the above assumption on the initial shape of the simulated molecular cloud should be reasonable. The mass of the cloud is uniformly distributed through a sphere of radius R . In the simulation we choose the middle finger of the Eagle nebula as an example since it has a simpler structure than the other fingers (White et al. 1999). The initial geometric and ultraviolet radiation field configurations of the simulated cloud are shown in Fig. 1.

For the head structure of the middle finger of the Eagle nebula, with a mass $\sim 31 M_{\odot}$ and a temperature of 20 K, the Jeans length $R_J = 0.2 \text{ pc}$. However, the radius of the head structure is about 0.1 pc, which means that the structure is unstable against the self-gravity of the cloud according to the Jeans criteria. A simple SPH simulation reveals that it would collapse in $< 10^5 \text{ yr}$.

However, it is well known that molecular clouds are supported by turbulent and magnetic pressures in addition to the thermal pressure $P_{\text{th}} = nkT$. In the case of the Eagle nebula, the observational results show that a large-scale ordered magnetic field is not likely to produce sufficient internal pressure balancing the external pressure and there may be a disordered component of magnetic field which provides an isotropic pressure to balance the external pressure in the head structure (White et al. 1999). The relevant turbulent pressure

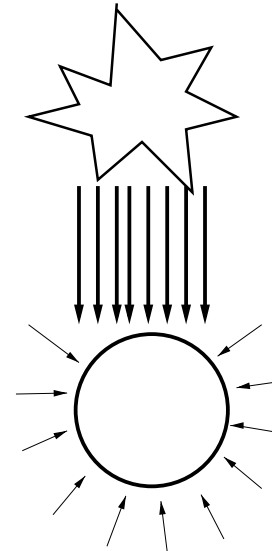


Figure 1. The initial geometric and the surrounding ultraviolet radiation configurations. The heavy arrows represent the strong Lyman continuum flux from the massive stars above the molecular cloud, and the short arrows represent the isotropic FUV radiation ($h\nu < 13.6 \text{ eV}$) flux from the interstellar medium environment.

P_{tb} and the induced isotropic pressure P_B due to the magnetic field are related to the thermal pressure by two dimensionless parameters (Gorti & Hollenbach 2002),

$$\alpha = \frac{P_{\text{tb}}}{P_{\text{th}}}; \quad \beta = \frac{P_B}{P_{\text{th}}}. \quad (13)$$

The internal pressure of the molecular cloud then consists of three terms:

$$P = (1 + \alpha + \beta)P_{\text{th}}. \quad (14)$$

Observations of molecular clumps in star-forming regions (Jijian, Myers & Adams 1999) indicate that the values of α range from about 0 in cold, dark clouds to ≥ 2 in regions of massive star formation. There is also observational evidence to suggest that turbulent support in clumps decreases on the smaller scales of star-forming clumps with a diameter ≤ 0.2 pc, where $\alpha \leq 2$ (Goodman et al. 1998). Therefore we adopt the value of $\alpha = 2$ in our simulations considering that the actual diameter of the condensed head at the tip of the middle finger is 0.2 pc.

Measurements of magnetic fields and hence β are difficult to make, but present observational data suggest a wide range of values for β , ranging from 0 to a few (Crutcher 1999). We take β as a parameter in our simulations and determine a proper value of β for the Eagle nebula so that the total internal pressure can balance the self-gravity when the ultraviolet radiation has not been switched on in order to observe the effect of ultraviolet radiation triggered star formation in a molecular cloud. A value of $\beta = 6$ is then obtained in this way.

We start with a warm spherical cloud of mass $68 M_{\odot}$ and temperature 60 K. The initial radius of the cloud is 0.4 pc and it is assumed to have a uniform mass distribution and zero velocity distribution.

The boundary condition adopted is of constant external pressure which corresponds to an external medium composed primarily of atomic hydrogen with $n(\text{H I}) = 10 \text{ cm}^{-3}$ and $T = 100 \text{ K}$.

With these implementations of the original SPH code, we have developed a comprehensive three-dimensional SPH code of the RDI effects of young stars on their natal molecular clouds, which allows a detailed investigation of both the dynamical and thermal evolution of a molecular cloud under the influence of nearby massive stars in a more accurate and realistic way than other existing models, because our model self-consistently includes most of the necessary physical processes which are universal in astrophysical environments.

In the following subsections, we present and discuss the results from the simulations based on the above-described model with 20 000 simulated particles applied.

3 RESULTS AND DISCUSSION

3.1 The dynamical evolution of the simulated molecular cloud

Figs 2, 3 and 4 together show the number density evolution of the spherical molecular cloud with the initial conditions stated in Section 2.4. The overall evolutionary process can be categorized by three different stages according to the configuration of the simulated molecular core. In order to distinguish different morphologies of the core, we define a flat/elongated core as an object with horizontal dimension bigger/smaller than the vertical dimension.

(i) *Flat core formation stage.* The left-hand panel in Fig. 2 shows the number density distribution of the simulated cloud at an early time $t = 4300$ yr. When the intensive Lyman continuum flux from nearby massive stars falls on to the surface of the upper hemisphere of the cloud (front surface) as shown in Fig. 1, the gas within a thin

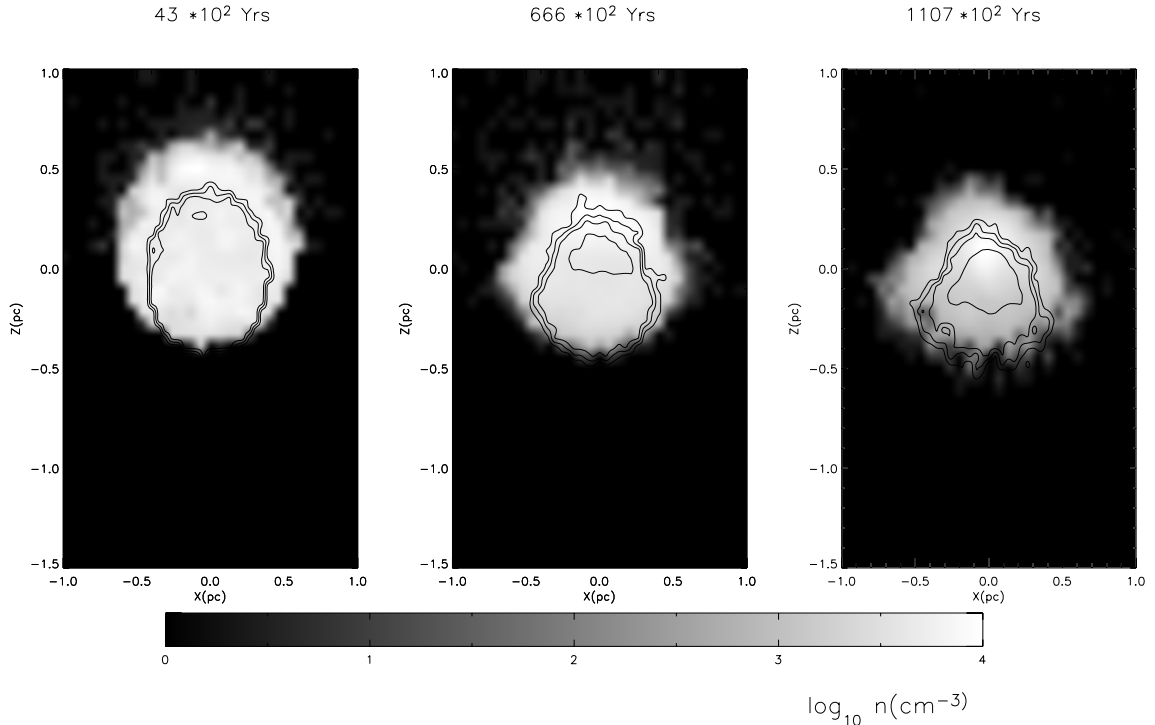


Figure 2. The evolution of the hydrogen number density n (cm^{-3}) of the simulated molecular cloud from early stages $t = 4300$ yr to 0.11 Myr, when a flat core has formed in the front part of the cloud. The z -axis is along the strong radiation flux from the massive stars, and the x -axis is in the plane perpendicular to z . The initial centre of the cloud is at $(x, z) = (0, 0)$.

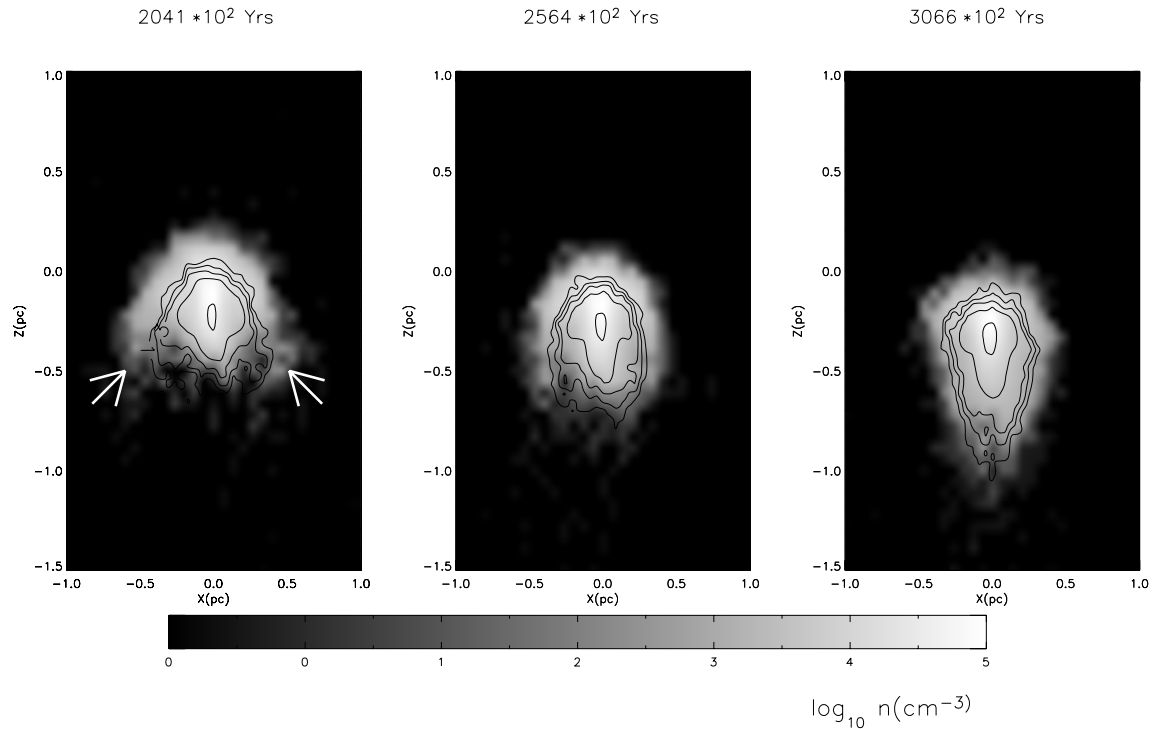


Figure 3. The evolution of the number density n of the simulated molecular cloud over the period $t = 0.2\text{--}0.3$ Myr, when the core gradually becomes elongated. The white arrows point to the location of the ‘ear-like’ structures.

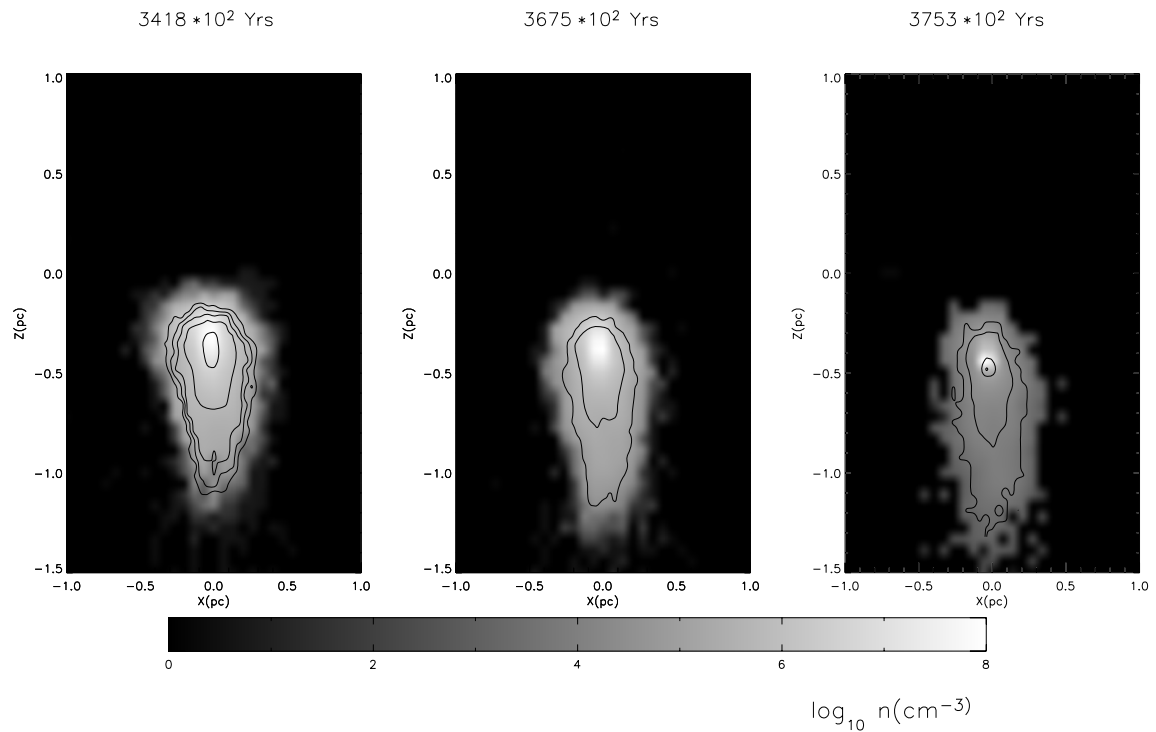


Figure 4. The final evolutionary stages of the condensed core collapsing into triggered star formation after 0.375 Myr.

layer at the surface of the upper hemisphere is ionized and forms an ionization front at the front surface. The ionized gas is heated during the ionization and the temperature increases. The increased pressure due to the temperature increase at this top layer drives an isothermal shock into the cloud, which compresses the neutral gas

ahead of it (i.e. below the front surface). The contour lines at the front surface layer of the cloud in the left-hand panel in Fig. 2 show that a density gradient has built up there. The increased density in the neutral gas leads to a rapid mass accumulation to form a condensed core. In Fig. 5, the accumulated mass in a volume of

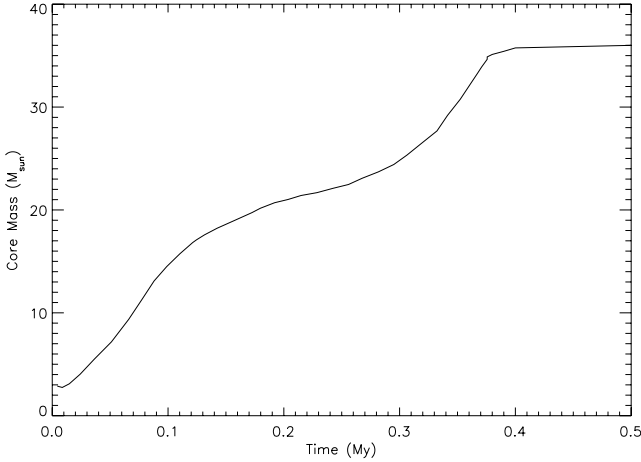


Figure 5. The evolution of mass accumulated into the core of dimension $0.2 \times 0.2 \times 0.35 \text{ pc}^3$ centred at the densest point in the simulated molecular cloud.

$0.2 \times 0.2 \times 0.35 \text{ pc}^3$ (similar dimensions to the condensed core at the head of the middle finger of the Eagle nebula) centred at the densest point in the cloud is shown as a function of time over the whole simulation period. The mass accumulation rate in the specified volume is about $93 M_{\odot} \text{ Myr}^{-1}$ in the first few thousand years. On the other hand, the ionized and heated gas at the cloud surface flows radially away from the surface of the cloud and forms an evaporating layer surrounding the surface of the cloud, shown as the ‘atmosphere’ outside these contour lines in the left-hand panel of Fig. 2.

The above-mentioned shock compression and gas evaporation can be observed from the surface of the rear hemisphere as well, but the effect is much weaker than that at the front hemisphere, because the heating effect of photoelectric emission of electrons from dust grains is much weaker than that of hydrogen ionization by Lyman continuum radiation.

At time $t = 0.666 \times 10^5 \text{ yr}$, the compressed layer (shock front) leading the ionization front moves toward the rear hemisphere, while a flat core starts to form in the front hemisphere of the cloud due to the shock, as shown in the middle panel of Fig. 2. During the next $5 \times 10^4 \text{ yr}$, the core is continuously compressed and becomes flattened owing to shock compression when $t = 1.107 \times 10^5 \text{ yr}$, as shown in the right-hand panel of Fig. 2.

With further compression of the core, as shown in the left-hand panel of Fig. 3, small ‘ear-like’ structures (indicated by the white arrows) similar to those in the Lefloch & Lazareff (1994) simulations appear from the two sides of the cloud structure where the compressed layer meets the gas particles at the rear edge of the cloud at $\theta \sim 90^\circ$. A small ‘nose’ structure also grows from the rear edge of the cloud along the central line $x = 0$, which is due to the maximum ionization effect along the surface normal direction. Despite the appearance of the ‘nose’ structure from the central line, the morphology of the cloud and the core are still in a flat shape which is outlined by the contour lines in the left-hand panel of Fig. 3. In the next few $\times 10^4 \text{ yr}$, the ‘ears’ gradually merge with the ‘nose’ structure in the centre and, when $t = 2.564 \times 10^5 \text{ yr}$, the ‘ears’ finally disappear and a flat core with a ‘nose’ structure along the centre line is shown in the middle panel in Fig. 3. Now the whole cloud has a quasi-spherical morphology. In Section 3.2.1 we will present a detailed discussion on the mechanism for the formation of the ‘ear’ and ‘nose’ structures.

(ii) *Elongated core formation stage.* In the next stage of the evolution of the simulated cloud, the whole molecular cloud structure gradually becomes elongated, as shown in the right-hand panel of Fig. 3 when $t = 3.066 \times 10^5 \text{ yr}$. At the time $t = 3.418 \times 10^5 \text{ yr}$, as shown in the left-hand panel of Fig. 4, a finger structure appears. A dense and elongated core having a radius of 0.1 pc in the plane perpendicular to the ionizing flux direction and a length of 0.35 pc along the ionizing flux direction forms, as shown in the left-hand panel of Fig. 4. The mass included in the above core is about $31 M_{\odot}$, and the average hydrogen number density is about 10^5 cm^{-3} . The configuration of the simulated molecular cloud at this stage is very similar to the head structure of the middle finger observed by White et al. (1999). We will further discuss other physical features of the cloud structure at this moment of time in the following sections.

(iii) *Triggered star formation stage.* At $t = 3.675 \times 10^5 \text{ yr}$, a highly condensed spherical core starts to form at the head of the elongated structure due to the self-gravity of the core, as shown in the middle panel of Fig. 4. With further condensation of the gas into the centre of the spherical core, the hydrogen density n in the centre of the core increases dramatically, reaching 10^8 cm^{-3} when time $t = 3.753 \times 10^5 \text{ yr}$. The mass accumulated in the condensed elongated core ($0.2 \times 0.2 \times 0.35 \text{ pc}^3$) reaches $34 M_{\odot}$ when $t = 3.753 \times 10^5 \text{ yr}$ through compression by the isothermal shock induced by the ionizing radiation, which causes the mass to condense and then collapse into the centre by gravitation, i.e. triggers the next generation of star formation in the centre. The material in the condensed core quickly collapses into a smaller sphere with a radius of 0.06 pc and a mass of about $25 M_{\odot}$.

The final mass of the whole finger structure is $\sim 60 M_{\odot}$. In the whole evolutionary process, the molecular cloud has lost a mass of $8 M_{\odot}$ through photoevaporation over 0.39 Myr , which results in an average mass-loss rate of $8/0.39 \sim 20.5 M_{\odot} \text{ Myr}^{-1}$. This value is similar to the $21 M_{\odot} \text{ Myr}^{-1}$ that was obtained by Lefloch & Lazareff’s simulation (Lefloch & Lazareff 1994). In the next section, we will discuss the mechanism for the appearance of different morphologies of the cloud during its evolution.

3.2 The dynamical evolution of the cloud structure

In observing the changes in the morphology of the cloud structure, we are interested in the features of growth of the ‘ears’ and ‘nose’ structures and also the time durations that the cloud structures stay in the ‘flattened core’ and ‘elongated core’ stages. We will discuss them by examining the evolution of the configuration of the velocity field shown in Fig. 6, which reveals an approximate evolutionary picture of the momentum of the cloud structure.

3.2.1 The growth of the ‘ears’ and ‘nose’ structures

At early evolutionary stages, while the ionized gas at the top layer of the front surface of the spherical cloud is heated and evaporated from the surface, an isothermal shock travels in the opposite direction towards the rear part of the cloud and compresses the neutral gas ahead, shown as in the top left-hand panel in Fig. 6. The high-pressure induced velocity distribution $V_z(\theta)$ at the front surface layer is approximately given by (Lefloch & Lazareff 1994)

$$V_z(\theta) = V_z(0)(\cos \theta)^{1/4}, \quad (15)$$

where θ is the angle at a surface point $r = R$ from the z -direction, and $V_z(0)$ is the velocity at the point $r = R$, $\theta = 0$, which is 7.5 pc Myr^{-1} (7.4 km s^{-1}) at the time $t = 4300 \text{ yr}$. The gas close

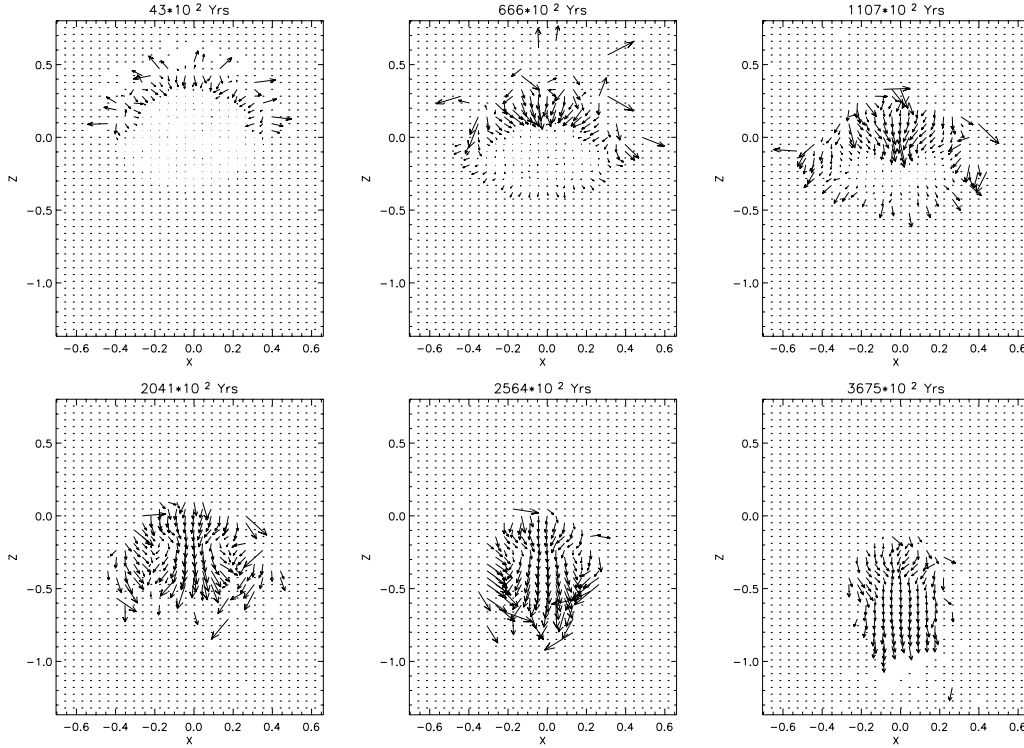


Figure 6. The velocity field evolution of the simulated cloud over a time period of 0.37 Myr. The length of the arrows indicates the magnitude of the velocity and the longest arrow represents a velocity of $+28 \text{ km s}^{-1}$.

to the symmetry axis ($x = 0$) has a smaller θ at the front surface layer and will move forward faster than the gas that lies further away (larger θ) from the axis $x = 0$. This velocity gradient over θ causes the deviation of the morphology of the front surface of the cloud from the hemisphere, i.e. the front surface of the hemisphere becomes squashed, which can be seen from the middle panel in Fig. 2.

The gas particles close to the outermost parts of the cloud ($\theta \sim 90^\circ$), as shown in the top middle and top right-hand panels in Fig. 6, obtain an extra velocity along the z -direction due to the non-radial isothermal shock compression, so that they intersect the rear edge of the cloud and form the ‘ear-like’ structures on the two sides of the cloud, which are shown in the left-hand panel of Fig. 3.

Also the gas near the symmetry axis ($x = 0$) progresses forward to the rear hemisphere much faster than that further from the symmetry axis because of its higher velocity obtained from the radiation-induced compression, so that a ‘nose’ gradually grows out from the shock front along the $x = 0$ axis over the next $0.44 \times 10^5 \text{ yr}$, dragging most of the mass of the cloud with it, as shown clearly in the top right-hand panel of Fig. 6.

In the following evolutionary stages, after the gas in the ears passes the front hemisphere, they will merge into the moving nose structure along the $x = 0$ axis because the effect from the ionization flux is greatly decreased inside the core region and the gravitational force of the nose structure becomes more important so that the gas in the ‘ears’ converges into the ‘nose’ structure. This effect can be seen from the bottom left-hand and bottom middle panels of Fig. 6 by the directions of the velocities of the gas in the ‘ears’ pointing to the nose. The ‘ears’ merging with the moving ‘nose’ gradually create the tail structure of the cloud complex.

The average velocity gradient in the dense core in the left-hand panel of Fig. 4 (which corresponds to the current state of the

observed head structure of the Eagle nebula) is $\partial v / \partial r \sim 1.88 \text{ km s}^{-1} \text{ pc}^{-1}$, which is consistent with the observed value of $1.7 \text{ km s}^{-1} \text{ pc}^{-1}$ (White et al. 1999). The compressed gas left in the head of the cloud complex now has reached a density that exceeds its Jeans density so that it collapses into a dense core to form a new star there, while the whole cloud complex keeps moving forward along the $-z$ -direction because of the ‘rocket effect’ (Oort & Spitzer 1955) arising from the evaporating gas leaving the front surface of the cloud, as shown in the bottom right-hand panel of Fig. 6. This ‘rocket effect’ makes the mass centre of the cloud complex move a distance of 0.4 pc over a period of 0.37 Myr.

3.2.2 The duration of the flat and elongated morphologies

Some of the above morphological features can be found in the Lefloch & Lazareff (1994) model as well, e.g. the ‘ear’ structures, and the elongated cloud complex (or cometary) morphology formed at the final stage of the evolution of the cloud. However, we cannot ignore some profound differences in the simulated morphologies presented by these two models. First, in our simulations, the ‘ear’ structures do not last as long as in Lefloch & Lazareff’s model, which we think may be consequences of (i) inclusion of gravitation in our model, and (ii) the three-dimensionality of our model, so the gas in the ‘ears’ in our model converges into the symmetry axis $x = 0$ much earlier than that in Lefloch & Lazareff’s model (which is clearly seen by the directions of the velocities of the gas in the ears), which results in the fact that the cloud complex stays longer in a flat-core morphology in our simulations. As can be seen from Figs 2–4, the ratio of the time that the cloud complex stays in the flat-core morphology to that in the elongated-core morphology is $\sim 2.4/3.9 \sim 62$ per cent, which means that the simulated

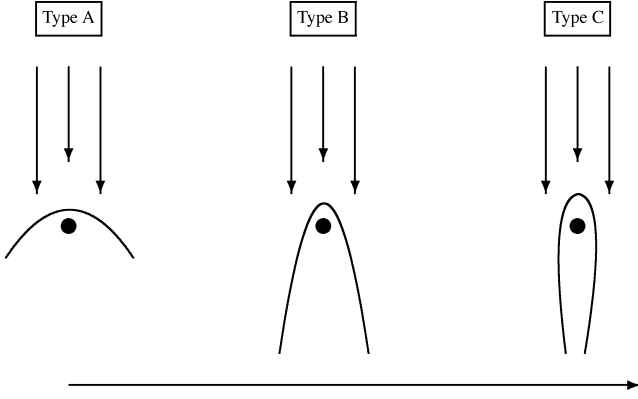


Figure 7. A schematic of three BRC morphologies. The vertical arrows represent the incoming ionizing photon flux and the horizontal arrow denotes the direction of the possible time evolution of the cloud complex under the influence of the ionizing radiation flux. The three types A, B and C correspond to the three morphologies in three different stages over the evolution of the cloud complex.

BRC spends 63 per cent of its lifetime in a type A (with a flat core) morphology, and $\sim(3.9 - 2.4)/3.9 \sim 37$ per cent of it in types B and C (with an elongated core), before it develops further to form a cometary structure or collapse to form a new star. We reach a similar conclusion from the results of a series of simulations performed for clouds of different masses. According to the statistical average principle, the above results mean that we should expect to find twice as many flat-core BRCs as elongated-core BRCs when we observe a big group of BRCs in a similar astrophysical environment. In comparison, the relevant two-dimensional modelling (Lefloch & Lazareff 1994, 1995) gave a value of $\sim 0.126/0.37 \sim 34$ per cent for the time duration of the type A morphology.

The above simulated morphological sequence of the cloud complex has been validated by many observations. Sugitani, Fukui & Ogura (1991; SFO) and Sugitani & Ogura (1994) classified their 89 observed BRCs (the SFO southern catalogue) into types A, B and C with an increasing curvature of the cloud rim, as shown in Fig. 7, which also roughly corresponds to the three stages in our simulated BRC evolutionary morphologies. It is found that the majority of BRCs (66 per cent) in the SFO southern catalogue are type A clouds, the remaining 37 per cent being types B and C. Our latest radio continuum and molecular line observational study of BRCs reveals a very similar BRC morphological distribution to that of Sugitani et al. (Urquhart et al. 2003, 2006). A further investigation of the structure of BRCs (Ogura & Sugirani 1998) supported by photoionization-induced shock models (Vanhala & Cameron 1998) also suggested that the above three morphological BRC types are possibly a time-evolutionary sequence. Therefore the above interpretation of our simulated results on the morphological evolution of a BRC can be well supported by observations. The value of 63 per cent for the ratio of the number of flat-core BRCs to that of elongated-core BRCs is consistent with the observational value of 66 per cent.

In order further to determine the role played by gravity in the triggered star formation process within the BRCs, we repeat the simulation without including gravity in the code. The result reveals similarities to those from the simulations of Lefloch & Lazareff (1994) and Williams et al. (2001), i.e. (i) the core has a shorter time duration in a flat-core morphology than that with gravity included; (ii) the core will not collapse and after $4-5 \times 10^5$ yr it stays in an equilibrium state with an average number density of 10^5 cm^{-3} and a

central density of up to 10^6 cm^{-3} . Therefore self-gravity of the cloud indeed plays an important role in triggered star formation under the influence of an ultraviolet radiation field. We will present more simulation results and analysis in our next paper for the discussion of the relationship between the morphology of the BRCs and the initial structure of the cloud.

3.3 The propagation of the shock and the ionization front

An important issue in the investigation of the star formation within the Eagle nebula fingers is to examine whether the propagation of the shock induced by the ionizing radiation into the structure has triggered an irreversible collapse of the molecular cloud into a condensed centre. From the simulated results, it is possible to study the propagating process of the shock by observing the evolution of the number density distribution n in the cloud structure.

In Fig. 8, snapshots of the distribution of the number density n and the ionization ratio x along the centre line of the structure at different times are shown. The left-hand panel of the first row shows that at a very early stage ($t_1 = 0.0043$ Myr), the gas in the cloud is pushed towards the centre not only from the front surface but also from the rear surface because of the surrounding weaker ultraviolet radiation from the interstellar medium. The ionization ratio x at the front surface reaches a peak value of 0.58. Since the ionization ratio x is linearly related to the ionizing flux J_0 , a sharp ionization front is built up instantly. The hydrogen ionization heating greatly increases the temperature at the front surface which results in a high pressure so that a strong compressive shock is formed at the front surface of the structure, as shown in the right-hand panel of Fig. 8. The bottom two panels show that the shock continues leading the ionization front into the cloud centre at $t_3 = 0.11$ and $t_4 = 0.2$ Myr respectively.

Overall, the head of the finger becomes denser and denser under the effect of the ionization-induced shock compression. With the increased density towards the centre of the head, the ionizing flux decreases very quickly [$J(z) \sim J_0 e^{-\sigma n(1-x)z}$], which results in a rapid drop of ionization ratio x inside the head structure.

If we define the region with highest density in the density profile as the shock front, the average speeds of the shock front are $v_s = 0.33, 0.22$ and 0.15 km s^{-1} over the three periods of $t_2 - t_1$, $t_3 - t_2$ and $t_4 - t_3$, while the corresponding speeds for the ionization front are $v_i = 0.18, 0.165$ and 0.056 km s^{-1} respectively. It is shown that the propagations of both shock and ionization fronts slow down because of the increased density ahead. Since the ionization front speed $v_i < v_s$, so the gap between the ionization front and the shock front slowly increases. After $t \sim 0.36$ Myr, the gap reaches a value of 0.125 pc, which is consistent with the fact that the peak submillimetre continuum emission from the clumps is located at about 0.1 pc deeper into the fingers than their photoionized front surface (White et al. 1999). In the following section, more details about this displacement will be discussed.

3.4 The evaporation of the ionized gases: H II region

While the ionizing radiation induced shock precedes the ionizing front into the cloud structure, the ionized hydrogen atoms at the top layer of the upper hemisphere are heated and evaporated, and move away from the front surface of the cloud to form an H II region around the front surface of the cloud. Although the gas at the other sites of the surface other than the front sites is heated as well by the surrounding environmental FUV radiation through the photoelectric emission from the surfaces of dust grains, the heating effect is much

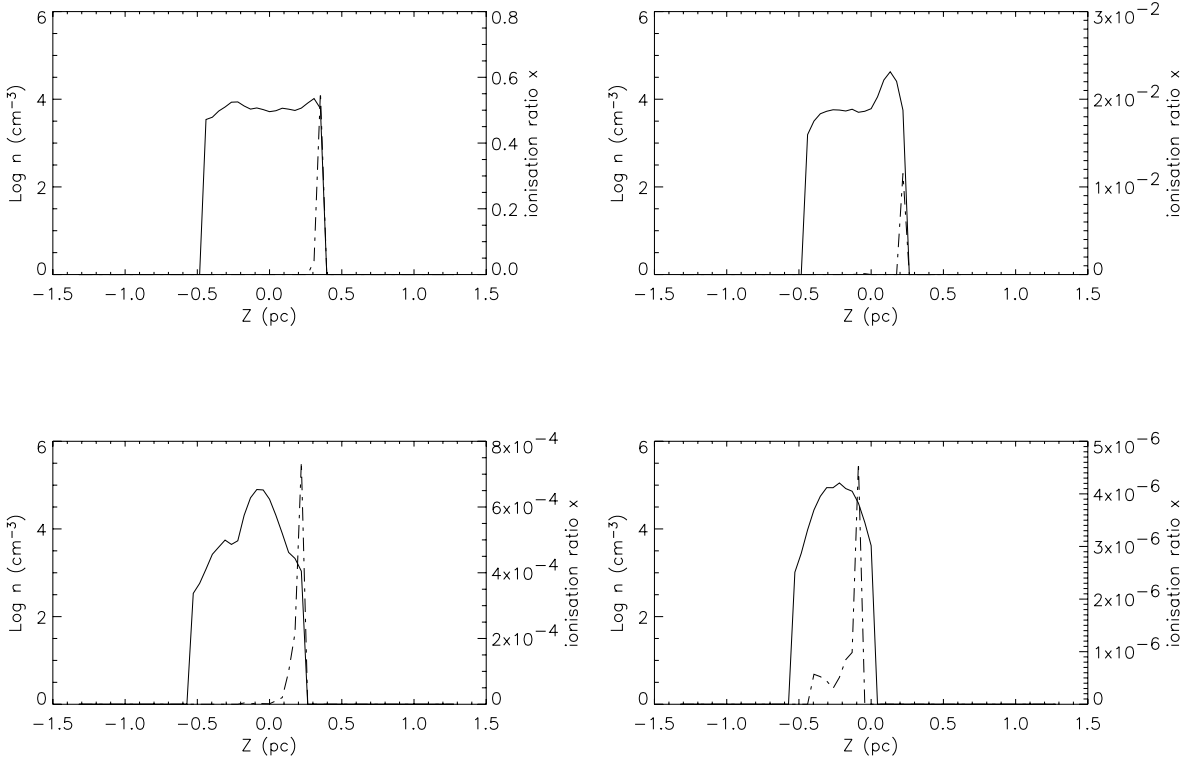


Figure 8. A shock (the peak of solid line) is leading the ionization front (dot-dashed line) moving into the molecular cloud. From left to right, top to bottom, are the density distributions in the cloud along the symmetrical axis $x = 0$ for the times $t = 0.0043, 0.067, 0.11$ and 0.2 Myr respectively.

weaker (because of the low abundance of the dust grains) when compared with that of hydrogen ionization so that the evaporating envelope is much thinner than that surrounding the front surface, as shown in Figs 2–4.

The panels in the upper row in Fig. 9 show the movement of this evaporating layer for the first few snapshots of $t = 0.0043, 0.009$ and 0.015 Myr. The average evaporation speed is about 25 km s^{-1} . From the bottom panels of the same figure, we can see that the temperature of this evaporating layer is about $6 \times 10^3 \text{ K}$, for which Hester et al. (1996) estimated a value of 10^4 K , and White et al. (1999) gave a value of 6700 K . The characteristics of the modelled H II region surrounding the front surface of the Eagle nebula finger fit well with the observed values.

3.5 Evolution of the temperature profile

The evolution of the temperature distribution of the head structure at times $t = 0.0044$ Myr (the dashed line) and 0.34 Myr (the solid line) along the centre line $x = 0$ are shown in Fig. 10. It is seen that shortly after the ionizing radiation is switched on, i.e. when $t = 0.0044$ Myr, the top layer at the front surface is heated as a consequence of hydrogen ionization heating, so that the temperature increases to $\sim 6000 \text{ K}$. Inside the structure the temperature is about 60 K , close to the initial temperature of the cloud, because the effect of the radiation has not yet penetrated. After the cloud has evolved for $t = 0.34$ Myr, the temperature in the surface layer of the cloud is about 200 K , since the ionization flux has greatly decreased at the surface of the cloud because of the ionization absorptions in the surrounding H II region (which is moving away from the main structure) for the recombinations of the electrons with the hydrogen ions. The temperature at the rear surface increases to a similar

value, due to the FUV radiation from the surrounding interstellar medium. The combination of the value of the surface temperature ($\sim 200 \text{ K}$) and the hydrogen density ($n \sim 5 \times 10^4$) yields a thermal pressure in the surface layer of $P_{\text{th}}/k = nT \sim 10^7 \text{ cm}^{-3} \text{ K}$. The total pressure $P/k \sim 7 \times 10^7 \text{ cm}^{-3} \text{ K}$ according to equation (15), which is in a good agreement with the observed value by Pound (1998). The temperature in the core region of $x \times y \times z = 0.2 \times 0.2 \times 0.35 \text{ pc}^3$, which is centred at $(x, y, z) = (0, 0, -0.43) \text{ pc}$, decreases to $13\text{--}18 \text{ K}$, below its original value of $T = 60 \text{ K}$, because of the enhanced radiation extinction, and the increased cooling efficiency in this higher density region.

In summary, the temperature distribution at the time $t = 0.34$ Myr describes a low-temperature ($13\text{--}18 \text{ K}$) core surrounded by an outer shell of warm material of temperature $200\text{--}250 \text{ K}$, which matches well with the the temperature characteristics of the observed head structure at the middle fingertip in the Eagle nebula (Pound 1998; White et al. 1999).

3.6 The main chemical abundance evolution

The initial conditions for all of the chemical abundances included are the same as those described in our previous paper, with $X(\text{C}^+) = X(\text{CO}) = X(\text{HCO}^+) = 0$ and $X(\text{C}) = X(\text{O}) = 10^{-4}$ when the simulation starts, where $X_i = n_i/n(\text{H}_2)$ (White et al. 1999). In the left-hand panel of Fig. 11, the distributions of the fractional abundances of carbon-bearing species are displayed for the time $t = 0.34$ Myr. In the densest region between $z = -0.5$ and -0.3 pc , carbon is mainly in the form of CO, which correlates with the density of H_2 because its production rate scales as $\propto n^2(\text{H}_2)$, which causes the peak to be deep inside the structure. Outside the core $z > -0.3 \text{ pc}$, C I and C^+ are of comparable abundance at the

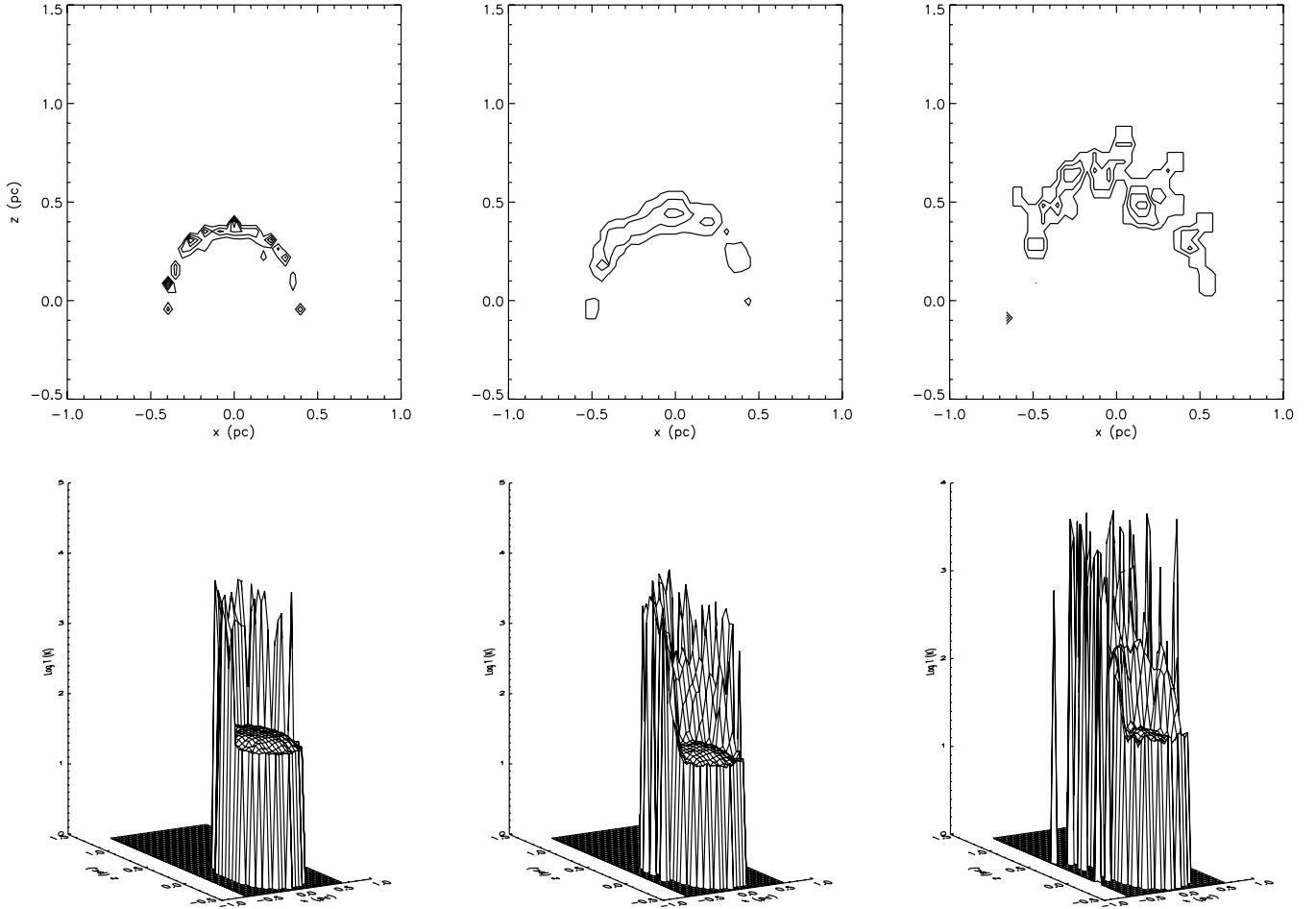


Figure 9. Top row: the ionized hot gas is leaving the upper semi-spherical surface. The contours are the values of the ionization rate x ; the biggest value is 0.58. The left-hand, middle and right-hand panels are the ionization rate distributions in the evaporating layer over the head of the middle finger of the Eagle nebula at times 0.0043, 0.009 and 0.015 Myr respectively. Bottom row: the temperature [$\log T$ (K)] distribution in the ionized hot gas over the same period of time.

front edge of the cloud structure, due to an increased ionization of C I into C⁺ which results in a dramatic increase in abundance of the latter. The peak of the ionization ratio x at $z \sim -2.7$ pc reflects the position of the bright rim. In other words, the ionization peak

is ahead of the CO peak by a distance of 1.25 pc, which provides a very consistent description of the relationship of the CO and H α distributions inside the cloud head with the observed displacement of 0.11 pc between CO line and H α line profiles (White et al. 1999).

The distribution of the HCO⁺ abundance shows a non-monotonic variation over the region because its production rate is dependent on the ionization flux, the H-bearing species and CO species. Near the front edge of the structure at $z = -0.3$ pc, these three factors cause a peak of the HCO⁺ production rate. Deeper inside the structure, the high abundance of CO is dominant in the production rate of HCO⁺, thus there is a similar pattern to that of CO, which is consistent with the observations of White et al. (1999).

White et al. also found that the ratio of C I/CO abundance increases in the low column density regions. The right-hand panel of Fig. 11 shows that the corresponding ratio increases dramatically in the front region of the head structure, where the density of the cloud is very low.

4 COMPARISON WITH THE RESULTS FROM THE PREVIOUS MODEL

First, we would like to point out that the estimated cloud thermal and chemical structures presented in the previous paper (White et al. 1999) were based on a static model under the assumption that the cloud was under hydrostatic equilibrium, i.e. the density

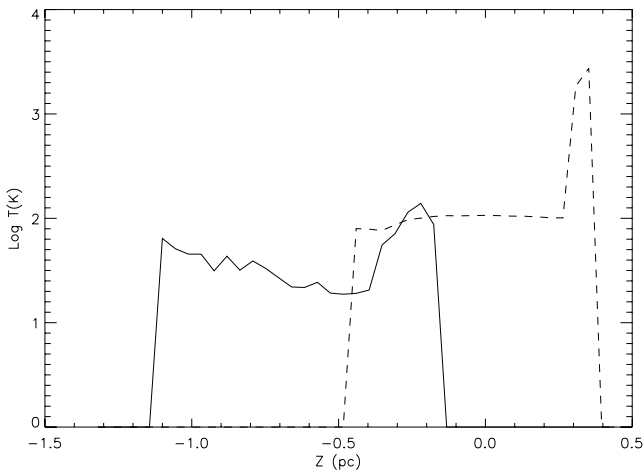


Figure 10. The temperature distributions at the initial and late stages of the evolution. The dashed line is for $t = 0.0044$ Myr, and the solid line is for $t = 0.34$ Myr.

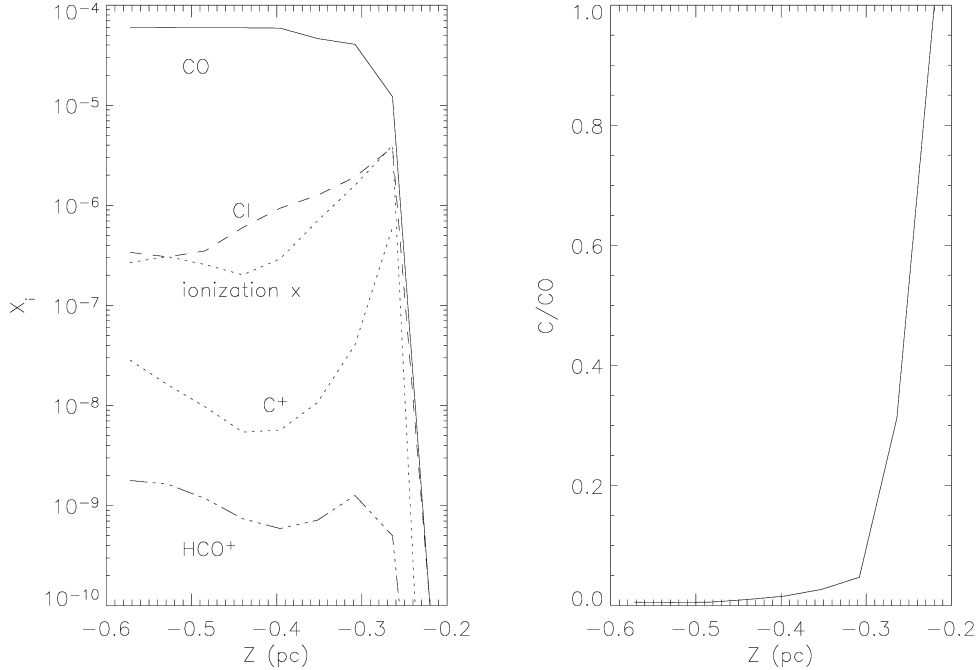


Figure 11. The main chemical distributions at the time $t = 0.34$ Myr.

distribution was fixed in time. Then the temperature and chemical profiles were estimated according to the thermal and chemical models described in the previous SPH code, which of course do not actually describe the dynamical evolution of the cloud structure.

Secondly, a dynamical simulation based on the previous SPH code in the absence of magnetic and turbulent pressure support indicates a quick collapse of a spherical molecular cloud of initial mass $68 M_{\odot}$ and radius 0.4 pc [or mass $31 M_{\odot}$ and radius 0.1 pc, as we have used in our previous paper (White et al. 1999)] in much less than 10^5 yr which is not a reasonable result for the Eagle nebula complex.

Thirdly, as we have mentioned in the previous sections, the previous SPH code did not include the Lyman continuum in the radiation field, and the consequent hydrogen ionization heating and cooling processes, so it greatly decreased the effect of radiative implosion on the BRC, because the temperature near the bright rim of the cloud can only be increased to 190 K by the photoelectric effect of the FUV radiation. With the inclusion of Lyman continuum radiation, the ionization heating can heat the front layer of the cloud up to 7000 K in the first few hundred years, a reasonable temperature for an H II region.

Therefore the simulation based on the previous SPH code can only simulate the effect of photoelectric heating of FUV radiation on the evolution of the molecular cloud, not the whole evolutionary picture of how a ubiquitous molecular cloud under the effect of nearby massive stars can evolve into a finger-like BRC with its life ending at triggered star formation, or formation of a stationary cometary structure, or being evaporated totally by the radiative field of the nearby massive stars. As we have shown in this paper, these effects can only be modelled via the comprehensively extended model.

5 CONCLUSION

With the inclusion of the Lyman continuum in the external radiation flux and hydrogen ionization heating effects in the energy equation in the previous code, and turbulent and magnetic pres-

ures in the internal pressure of the molecular cloud, the upgraded three-dimensional SPH model successfully describes the dynamical evolution of an initially spherical uniform molecular cloud into cometary/triggered star formation under the influence of the strong ultraviolet radiation from nearby stars plus isotropic surrounding interstellar medium radiation, and self-gravity of the molecular cloud.

The application of the model to an initially spherical molecular cloud of mass $68 M_{\odot}$ and temperature 60 K results in an Eagle nebula finger-like structure with a very dense core of dimensions $0.2 \times 0.2 \times 0.35$ pc³ and a mass of $31 M_{\odot}$ at its head after 0.34 Myr. The core has an average density of 10^5 cm⁻³ and a temperature of about 13 – 18 K with a velocity gradient of 1.91 km s⁻¹ at time $t = 0.34$ Myr. The dense core is surrounded by a warmer layer of temperature 200 – 250 K. The simulated H II region is of temperature 3 – 7000 K. The characteristics of the simulated chemical distributions are: (i) the CO abundance peak is 0.125 pc deeper into the core from the peak of the ionization fractional ratio x at the edge of the head structure; (ii) the HCO⁺ abundance follows a similar pattern to CO in the core region; (iii) the abundance ratio of C I/CO increases with the decrease of the column density of the cloud. The above-described characteristics of the simulated head structure coincide very well with the recent observational data (White et al. 1999). The simulation results also show that the core will collapse into its centre after another 7800 yr.

It is concluded that the radiation-induced compression wave has yet to pass the head structure and that the currently observed head structure at the tip of the middle finger is a part of an object which evolved from an initially larger and warmer pre-existing molecular clump. This cloud clump has been under the effect of strong ultraviolet radiation from nearby stars for about 0.34 Myr and is currently at a transition stage towards triggered star formation.

The simulation reveals some of the similar morphological structures in the evolutionary process of the molecular cloud to those displayed by Lefloch & Lazareff's two-dimensional model, and obtains a very similar estimate of the photoevaporation rate ($20 M_{\odot} \text{ Myr}^{-1}$ versus $21 M_{\odot} \text{ Myr}^{-1}$) from the surface of the front side, which

shows the reliability of our modelling. This also shows that Lefloch & Lazareff's two-dimensional model is appropriate to consider the photoevaporation of a BRC, but not the issue of triggered star formation in the cloud.

The estimate of the relative lifetimes of type A and type B/C BRCs shows that a BRC remains in type A morphology for nearly twice the time spent in type B/C morphology, which means that we should observe double the number of BRCs in type A morphology. This prediction agrees well with the observational results by Sugitani et al. (1991) and Urquhart et al. (2003, 2006), and thus provides a reasonable explanation for the observed outnumbered flat-core BRCs.

Comparing the above results with those based on the previous SPH model, we can conclude that hydrogen ionization heating by Lyman continuum plays a much more important role in the dynamical evolution of a molecular cloud than that of photoelectric heating by the surrounding interstellar medium radiation. Also the inclusion of the turbulent and magnetic field pressures in the molecular cloud in the upgraded model makes the model more realistic so that it can trace the origin of an observed cloud, reveal the whole dynamical evolution process of a molecular cloud to triggered star/cometary formation under the influence of nearby stars, and predict the future evolution of the observed object.

ACKNOWLEDGMENTS

We thank the anonymous referee for his/her helpful suggestions which have made the presented work more reliable, and also we learnt a lot from the communications with him/her.

REFERENCES

- Bertoldi F., 1989, *ApJ*, 346, 735
 Cantó J., Raga A., Steffen W., Shapiro P. R., 1998, *ApJ*, 502, 695
 Crutcher R. M., 1999, *ApJ*, 520, 706
 Désert F.-X., Boulanger F., Puget J. L., 1990, *A&A*, 237, 215
 Dyson J. E., Williams D. A., 1997, *The Physics of the Interstellar Medium*, 2nd edn. IoP Publishing, Bristol
 Fukuda N., Hanawa T., Sugitani K., 2002, *ApJ*, 568, L127
 García-Segura G., Franco J., 1996, *ApJ*, 469, 171
 Goodman A. A., Barranco J. A., Wilner D. J., Heyer M. H., 1998, *ApJ*, 504, 223
 Gorti U., Hollenbach D., 2002, *ApJ*, 573, 215
 Habing H. J., 1968, *Bull. Astron. Inst. Neth.*, 19, 421
 Hester J. et al., 1996, *AJ*, 111, 2349
 Hummer D. J., Seaton M. J., 1963, *MNRAS*, 125, 437
 Hurwitz M., Bowyer S., Martin C., 1991, *ApJ*, 372, 167
 Jijina J., Myers P. C., Adams F. C., 1999, *ApJ*, 125, 161
 Kessel-Deynet O., Burkert A., 2000, *MNRAS*, 315, 713
 Kessel-Deynet O., Burkert A., 2003, *MNRAS*, 338, 545
 Lefloch B., Lazareff B., 1994, *A&A*, 289, 559
 Lefloch B., Lazareff B., 1995, *A&A*, 301, 522
 McCaughrean M. J., Andersen M., 2002, *A&A*, 389, 513
 Nelson R. P., Langer W., 1997, *ApJ*, 482, 796
 Nelson R. P., Langer W., 1999, *ApJ*, 524, 923
 Ogura K., Sugitani K., 1998, *Publ. Astron. Soc. Aust.*, 15, 91
 Oort J. H., Spitzer L., Jr, 1955, *ApJ*, 121, 6
 Osterbrock D. E., 1974, *Astrophysics of Gaseous Nebulae*. W. H. Freeman and Company, San Francisco
 Pound M. W., 1998, *ApJ*, 493, L113
 Raga A. C., de Gouveia Dal Pino E. M., Noriega-Crespo A., Mininni P. D., Velázquez P. F., 2002, *A&A*, 392, 267
 Sugitani K., Ogura K., 1994, *ApJS*, 92, 163
 Sugitani K., Fukui Y., Ogura K., 1991, *ApJS*, 77, 59
 Sugitani K. et al., 2002, *ApJ*, 565, L25
 Thompson R., Smith B., Hester J. J., 2002, *ApJ*, 570, 749
 Urquhart J. S., White Glenn J., Pibratt G. I., Fridlund C. V. M., 2003, *A&A*, 409, 193
 Urquhart J. S., Thompson M. A., Morgan L. K., White Glenn J., 2006, *A&A*, in press
 Vanhala H. A. T., Cameron A. G. W., 1998, *ApJ*, 508, 291
 White G. J. et al., 1999, *A&A*, 342, 233
 Williams R. J. R., Ward-Thompson D., Whitworth A. P., 2001, *MNRAS*, 327, 788

This paper has been typeset from a $\text{\TeX}/\text{\LaTeX}$ file prepared by the author.